Journal of Functional Materials and Applied Engineering

Research Paper

Preparation of Polyethyleneimine-Grafted Sodium Lignosulfonate Microspheres and Their Methyl Orange Adsorption Performance over a Wide pH Range

Jessica Martin [1], **Thomas Lee** [2,*]

[1] Department of Sustainable and Bioinspired Materials, Max Planck Institute of Colloids and Interfaces, Am Mühlenberg 1, Potsdam 14476, Germany

[2] Department of Bioproducts and Biosystems, Aalto University, P. O. Box 16300, Espoo 00076, Finland

*Corresponding author: Martin_buss@uark.edu; lee3029vans@gmail.com

Abstract. Conventional adsorbents fail to meet the demands of green sustainable development, and suffer drawbacks including narrow applicable pH window, high temperature sensitivity and poor regeneration capacity. In this work, polyethyleneimine (PEI) was grafted onto sodium lignosulfonate (LS) via inverse suspension polymerization to synthesize bio-based microspheres (LSMs) capable of adsorbing organic dyes across a broad pH spectrum. A suite of physicochemical characterization techniques, including scanning electron microscopy (SEM), Fourier-transform infrared (FTIR) spectroscopy, and thermogravimetric analysis (TGA), was applied to thoroughly examine the synthesized microspheres. Owing to their textured surface topography coupled with a high density of surface amine functionalities, the LSMs demonstrated robust and stable sequestration of methyl orange (MO) across a broad pH spectrum spanning from 3 to 11. Systematic batch equilibrium and kinetic studies were subsequently executed to elucidate the governing parameters influencing the MO uptake capacity of these microspheres. Among the models tested, the measured data were most faithfully reproduced by the combination of the Langmuir isotherm and the pseudo-second-order kinetic equation, from which the monolayer uptake capacity of the adsorbent was determined to peak at 416.03 $mg \cdot g^{-1}$. Reusability tests further highlighted the durability of the material: over ten rounds of adsorption followed by desorption, more than 98% of the dye could still be eliminated. Spectroscopic evidence gathered from FTIR and X-ray photoelectron spectroscopy (XPS) sheds light on how the dye is captured — rather than relying on a single driving force, the LSM adsorbent binds MO molecules through several non-covalent forces acting in concert, namely electrostatic attraction, hydrogen bonding, π–π stacking, and van der Waals interactions.

Keywords: *sodium lignosulfonate; microspheres; adsorption; methyl orange*

Received on 02 July 2024, Accepted on 05 Nov 2024, Published on 15 Dec 2024

1 Introduction

The contamination of aquatic environments represents a pressing worldwide ecological challenge that endangers public health. Methyl orange (MO), a representative synthetic chromophore, constitutes a perilous component of industrial wastewater streams originating from sectors such as papermaking, textile fabrication, leather processing, and allied manufacturing industries. The majority of artificially synthesized colorants exhibit pronounced toxicity, suspected carcinogenicity, remarkable chemical persistence, and strong resistance to biological degradation. Adsorption-based methodologies have gained extensive acceptance as a remediation strategy for effluents generated by the printing and dyeing industries. This approach is broadly acknowledged as an environmentally benign, operationally straightforward, and highly effective purification technology capable of achieving substantial contaminant removal. The selection of adsorbents directly determines the overall wastewater treatment efficiency. Marey et al. fabricated polystyrene-coated silica nanoparticles via high internal phase emulsion templating, which achieved effective removal of methylene blue from wastewater. Castaldo et al. synthesized amino-functional hyper-crosslinked poly(vinylbenzyl chloride-divinylbenzene) resins featuring strong polarity and abundant micropores, which enhanced the adsorption affinity toward polar dyes. Nevertheless, most such adsorbents are derived from petrochemical feedstocks, which conflict with the green

low-carbon philosophy advocated by the dual-carbon goals. Moreover, their adsorption capacity, selective performance and applicable range still require further improvement, leading to unsatisfactory wastewater treatment outcomes. Therefore, developing eco-friendly, renewable high-efficiency adsorbents bears important practical significance.

With the exacerbation of environmental crises and depletion of fossil fuels, natural biomass materials have attracted extensive research interest. Numerous studies have explored the adsorption applications of biomass resources including cellulose, starch, chitosan, lignin and agricultural/forestry waste. In one representative study, chitosan was anchored onto the surface of natrolite-based composite membranes by Hussain et al., yielding a material effective for MO removal. In a separate effort, discarded cellulose fibers were converted by Sun Baofen et al. into nitrogen-functionalized porous carbon via a spray-drying route, and the resulting adsorbents proved suitable for treating wastewater contaminated with methyl orange. Cellulose, starch and chitosan-based adsorbents boast wide raw material sources and favorable biocompatibility, showing broad prospects in dye wastewater treatment. However, these materials are limited by single surface functional groups, insufficient structural modification and weak regenerability. As the second most abundant natural aromatic macromolecule after cellulose, lignin-derived adsorbents exhibit tremendous potential for environmental applications. Compared with cellulose, starch and chitosan adsorbents, lignin-based materials stand out for their unique aromatic backbone, abundant functional groups and excellent recyclability, which greatly expand their application scenarios in wastewater treatment. Unfortunately, lignin molecules tend to form large aggregates via intra- and intermolecular hydrogen bonding due to its complex amorphous three-dimensional framework, resulting in low specific surface area and insufficient active sites, thus deteriorating adsorption performance. To broaden the application scope of lignin adsorbents, low-cost, facile surface modification technologies are urgently required to endow lignin with superior dye uptake performance. Pan Chao et al. fabricated phenolated lignin-iron metal-organic frameworks via a one-step hydrothermal route for methyl orange adsorption, yet the material suffered low capacity and narrow pH applicability. The intrinsic molecular structure of lignin allows grafting, crosslinking and polymerization-based surface modification. Polymer microspheres have been widely used for organic dye removal owing to uniform particle size distribution, excellent dispersibility, fast diffusion and mass transfer performance.

In this work, polyethyleneimine was grafted onto sodium lignosulfonate via inverse suspension polymerization to fabricate bio-based LSM microspheres capable of adsorbing organic dyes over a wide pH window. The obtained LSMs possess uniform particle size and abundant positively charged amine functional groups with moderate surface roughness, which facilitate efficient diffusion and immobilization of MO molecules. To gauge how effectively the fabricated LSMs could capture methyl orange, sorption experiments were carried out in batch mode, and the resulting measurements were fitted against classical kinetic and isotherm frameworks so as to clarify the nature of the adsorption process. FTIR and XPS characterizations were further adopted to reveal the underlying adsorption mechanism between LSMs and MO molecules.

2 Materials and Experimental Methods

2.1 Experimental Materials

All chemicals were employed as received without further purification unless otherwise indicated. Sodium lignosulfonate (LS), polyethyleneimine (PEI, Mw = 70,000), and polyethylene glycol (PEG, M_n = 4,000) meeting analytical-grade specifications were sourced from Inokai Reagent Co., Ltd. Sodium dodecylbenzene sulfonate (SDBS), sodium alginate (SA), and methyl orange (MO) of analytical purity were furnished by Kelong Chemical Co., Ltd. (Chengdu). All chemical reagents employed in this work — liquid paraffin, epichlorohydrin (ECH), hydrochloric acid (HCl), sodium hydroxide (NaOH), absolute ethanol, and petroleum ether — were of analytical grade and supplied by Aladdin Biochemical Technology Co., Ltd., whereas the deionized water used throughout the experiments was prepared in the laboratory prior to use.

2.2 Experimental Procedures

2.2.1 Fabrication of LSM Microspheres

An inverse suspension polymerization strategy was adopted to prepare the LSMs, and the overall preparation route is depicted schematically in Figure 1. In the initial step, 0.75 g of LS powder was introduced into 15 mL of distilled water, followed by 30 min of magnetic stirring until a homogeneous solution was obtained. Thereafter, 3.0 g of PEI, 0.30 g of PEG4000, 0.3 g of SDBS, and 15 mL of a 1.5 wt% aqueous sodium alginate solution were sequentially charged into the aforementioned LS solution under uninterrupted stirring, and the blending was continued until a fully homogeneous state was realized. The mixed aqueous phase was dropwise added into 90 mL liquid paraffin, followed by 30 min emulsification under stirring. During emulsion stirring, 3.5 mL epichlorohydrin was dropwise introduced, and the copolymerization reaction proceeded at 60 °C for 2 h to form crude LSM microspheres. Following precipitation, the microspheres were collected by filtration and rinsed several times alternately with ethanol and petroleum ether; subsequent oven-drying at 60 °C for 3 h afforded the LSMs as dry powders.

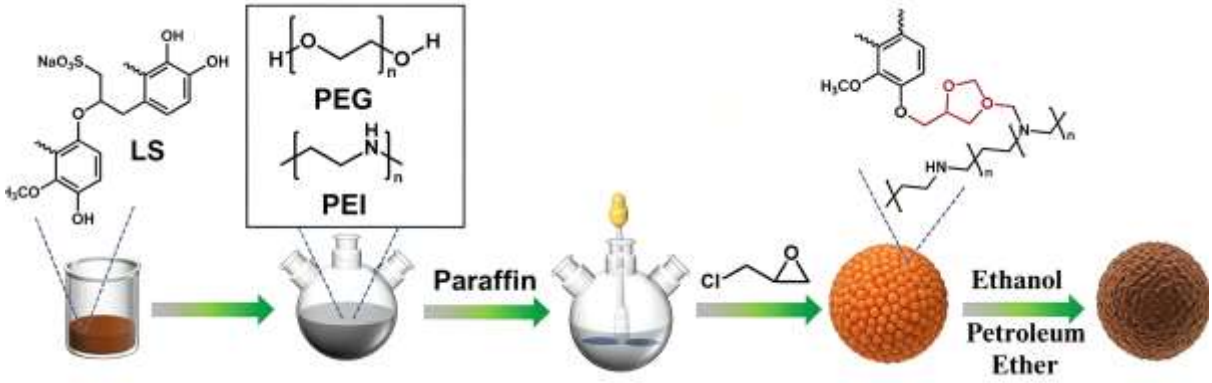

Figure 1 Flowchart for the preparation of LSM microspheres

2.2.2 Material Characterizations

The surface micromorphology of microspheres was observed using an Apreo S scanning electron microscope (FEI, USA). Ahead of morphological characterization, the freeze-dried microspheres were affixed to a conductive adhesive substrate and subsequently metallized with a thin gold layer via sputter deposition, with the electron beam operated at an accelerating potential of 15 kV.

FTIR characterization was performed using an IRTracer-100 spectrometer (Shimadzu, Japan), with specimens prepared through the KBr pellet technique. Each spectrum was obtained by averaging 32 individual scans, recorded over the 4000–400 cm^{-1} range with the resolution set to 4.0 cm^{-1}.

XPS analysis, conducted with a K-Alpha spectrometer (Thermo Scientific, USA), was employed to probe the elemental makeup of the LSM surfaces before and after MO uptake, using the neutral C 1s signal at 284.6 eV as the internal reference for binding energy correction.

Thermal stability of the samples was probed by TGA, in which specimens were ramped from 40 °C up to 700 °C at 10 °C/min while being purged with nitrogen.

The surface charge characteristics of the LSMs were evaluated on a Nano ZS90 Zetasizer (Malvern Panalytical, UK) by measuring the zeta potential of their diluted suspensions across pH 1–11; the desired pH values were established using 0.1 M solutions of HCl or NaOH.

2.2.3 Batch Adsorption Experiments

In the batch adsorption tests, LSM quantities ranging from 0.0025 to 0.05 g were weighed into 10 mL portions of MO solution whose initial concentration was fixed at C0=100 mg/L. Each mixture was then shaken for 2 h inside a thermostatted incubator operated at 25 °C and 200 $r \cdot min^{-1}$, a duration sufficient for equilibrium to be established between the adsorbent and the dye. Once the optimum adsorbent dosage had been identified, a

DOI:

series of independent batch tests was carried out to examine how solution pH (1–11), temperature (10–50 °C), and contact time (0–300 min) affected the adsorption performance. To examine whether the adsorbent could be regenerated and reused, it was subjected to 10 repeated cycles of adsorption followed by desorption, with 0.1 mol·L^{-1} acidic ethanol employed to strip the bound dye. At the end of each adsorption run, the solid–liquid mixture was filtered through a 0.22 μm PVDF aqueous membrane, after which the MO content remaining in the filtrate was quantified spectrophotometrically by reading its absorbance at 510 nm. On this basis, the removal efficiency of MO and the adsorption capacity at any given moment were computed from Equation (1) and Equation (2), respectively:

$$\text{MO Removal efficiency} = \frac{C_0 - C_t}{C_0} \times 100\% \quad (1)$$

$$Q_t \text{ Absorption capacity} = \frac{(C_0 - C_t)\,V}{M} \quad (2)$$

Where: C0: initial MO concentration, mg·L^{-1}; Ct: residual MO concentration at time t, mg·L^{-1}; Qt: adsorption capacity at time t, mg·g^{-1}; M: mass of LSM adsorbent, g; V: volume of MO solution, L.

3 Results and Discussion

3.1 Material Structural Characterizations

SEM images of raw LS and as-synthesized LSMs are presented in Figure 2(a) and (b). Both materials exhibit generally spherical particles with uniform size. Under identical magnification, raw LS particles show severe aggregation and smooth surface morphology, whereas LSM microspheres are well-dispersed with homogeneous particle sizes and negligible stacking, which provides larger contact area for MO molecules.

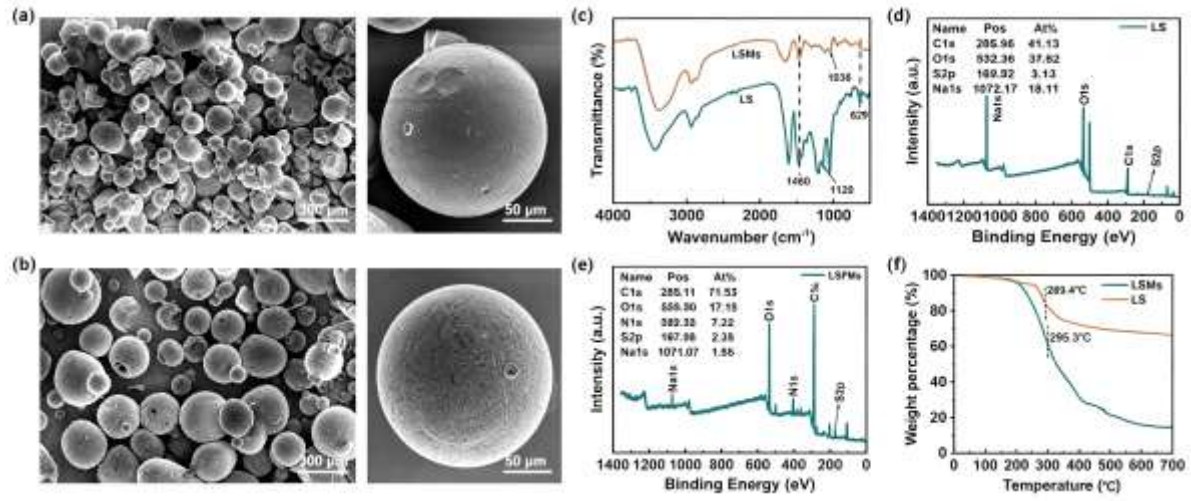

Figure 2 Structural characterizations of raw LS and LSM microspheres (a) SEM image of sodium lignosulfonate; (b) SEM image of LSM microspheres; (c) FTIR spectra of LS and LSMs; (d) XPS full spectrum of LS; (e) XPS full spectrum of LSMs; (f) TG thermograms of LS and LSMs

In Figure 2(c), the band appearing at 1605 cm^{-1} is attributed to vibrations of the aromatic skeleton, a feature shared by LS and the LSMs alike. Notably, a stretching band associated with C–N bonds arises at 1460 cm^{-1}, which corroborates the successful attachment of PEI-derived amine moieties to the LS framework. Moreover, the C–O stretching peaks of primary alcohols and phenols, originally located at 1120 cm^{-1}, vanish in the LSM spectrum, while a new C–N vibration band appears at 1036 cm^{-1}; together, these spectral changes substantiate the occurrence of the copolymerization reaction involving LS, PEI, and epichlorohydrin.Figure 2(d) and (e) present the full-scan XPS spectra of LS and LSMs, respectively. Both samples contain carbon, oxygen and sulfur elements. Sodium element accounts for 18.11 at% in LS due to its sodium lignosulfonate structure, while a nitrogen content

of 7.22 at% is detected in LSMs, which originates from grafted PEI chains and further validates successful preparation of PEI-modified lignin microspheres.

TGA curves in Figure 2(f) reveal distinct thermal decomposition behaviors. The mass loss of LS starting at 289.4 °C corresponds to thermal degradation of lignin skeletons, with a residual mass fraction of 66.37% at 700 °C. LSMs exhibit an additional thermal decomposition stage centered at 295.3 °C assigned to the crosslinked LS-PEI network, leaving only 14.52% residual mass at 700 °C. The mass difference indicates that PEI accounts for approximately 51.85% of the total mass of LSM composites.

3.2 Adsorption Performance of LSMs

3.2.1 Effect of Adsorbent Dosage

The relationship between the quantity of LSMs and the extent of MO capture is presented in Figure 3(a). Raising the adsorbent loading leads to a steady enhancement in dye removal, a trend explained by the correspondingly larger population of active sites exposed for MO binding. At a loading of 0.0075 g in 10 mL of MO solution, the removal of MO already surpasses 98%. Further increasing the dosage to 0.0125 g only improves the removal rate by merely 1.42%, as most active sites are already occupied. The capacity per unit mass, however, follows an opposite trend, declining as more adsorbent is introduced at a constant initial MO concentration. Taking both removal efficiency and capacity into account, 0.0075 g per 10 mL was selected as the optimal dosage of LSMs.

3.2.2 Effect of Temperature

The effect of temperature on MO uptake within the interval of 10–50 °C is presented in Figure 3(b). The adsorption capacity slightly increases with elevated temperature while maintaining nearly 100% removal efficiency throughout the tested range. Higher thermal motion accelerates molecular collisions between MO anions and LSM surfaces, facilitating the adsorption process. The material demonstrates favorable temperature tolerance for practical wastewater treatment.

3.2.3 Effect of Solution pH

UV-Vis absorbance curves and corresponding solution photographs under different pH values are shown in Figure 3(c). At pH = 1 and 2, significant absorbance signals of MO are detected at 510 nm.

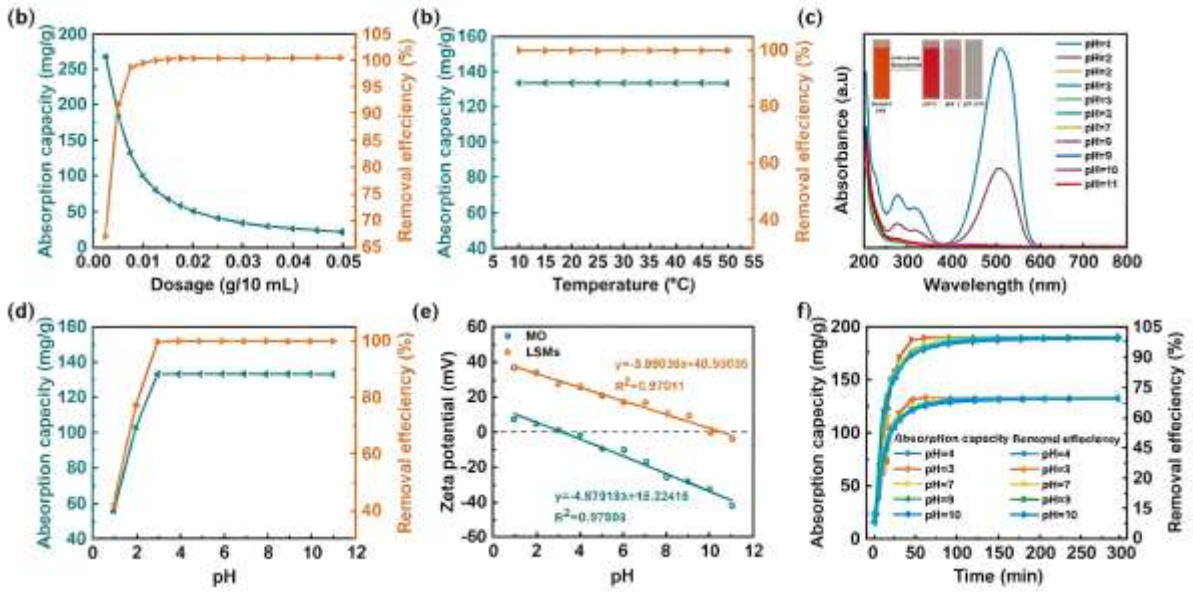

Figure 3 Adsorption performance of LSM microspheres toward methyl orange (a) Influence of adsorbent dosage; (b) Influence of temperature; (c) UV-Vis spectra and solution photographs at different pH; (d) Adsorption capacity and removal efficiency versus pH; (e) Zeta potential curves of LSM

and MO as a function of pH; (f) Adsorption kinetic profiles under different pH conditions

When pH is adjusted to 3–11, the absorbance nearly drops to zero, and the orange-red dye solution becomes transparent, indicating outstanding MO removal capacity in this broad pH window. Zeta potential test results (Figure 3(e)) show that the isoelectric point of LSMs is 10.6, while that of MO anionic dye is 3.1. Throughout the pH window of 3–11, the microspheres carry a positive surface charge while MO exists in anionic form, and the resulting strong electrostatic attraction between the two accounts for the highly efficient dye capture. The kinetic profiles recorded at different pH values (Figure 3(f)) show that most of the MO is taken up during the first 45 min, with equilibrium being essentially reached after 90 min at a removal efficiency above 99%. The above results prove that LSMs can efficiently eliminate MO contaminants over a wide pH range and possess promising prospects for dye wastewater remediation.

3.3 Adsorption Kinetics

Three kinetic frameworks — the pseudo-first-order model, the pseudo-second-order model, and the intra-particle diffusion model — were fitted to the time-resolved adsorption data in order to gain a quantitative understanding of the uptake dynamics; their respective linearized expressions are presented as Equation (3)–(5):

$$\ln\ (q_e - q_t) = \ln q_e - k_1 t \quad (3)$$

$$\frac{t}{q_t} = \frac{t}{q_e} + \frac{1}{k_2 q_e^2} \quad (4)$$

$$q_t = k_i t^{1/2} + c \quad (5)$$

Where: qt: instantaneous adsorption capacity at time t, $mg \cdot g^{-1}$; qe: equilibrium adsorption capacity, $mg \cdot g^{-1}$; k1: pseudo-first-order rate constant, min^{-1}; k2: pseudo-second-order rate constant, $g \cdot (mg \cdot min)^{-1}$; ki: intra-particle diffusion constant, $mg \cdot (g \cdot min^{1/2})^{-1}$; c: constant related to boundary layer thickness.

The time-dependent profile in Figure 4(b) can be resolved into two consecutive regimes: within the opening 45 min, a fast surface adsorption event already accounts for 87.04% of the total MO captured, after which the process transitions into a diffusion-limited regime that continues until equilibrium is established, at which stage over 92% of the dye has been immobilized. Table 1 lists the parameters extracted from the kinetic fits. Of the three models compared, the pseudo-second-order equation reproduces the data most faithfully, returning the largest correlation coefficient R^2=0.99932; this outcome points to chemical interaction as the rate-governing factor in the binding of MO to the LSMs.

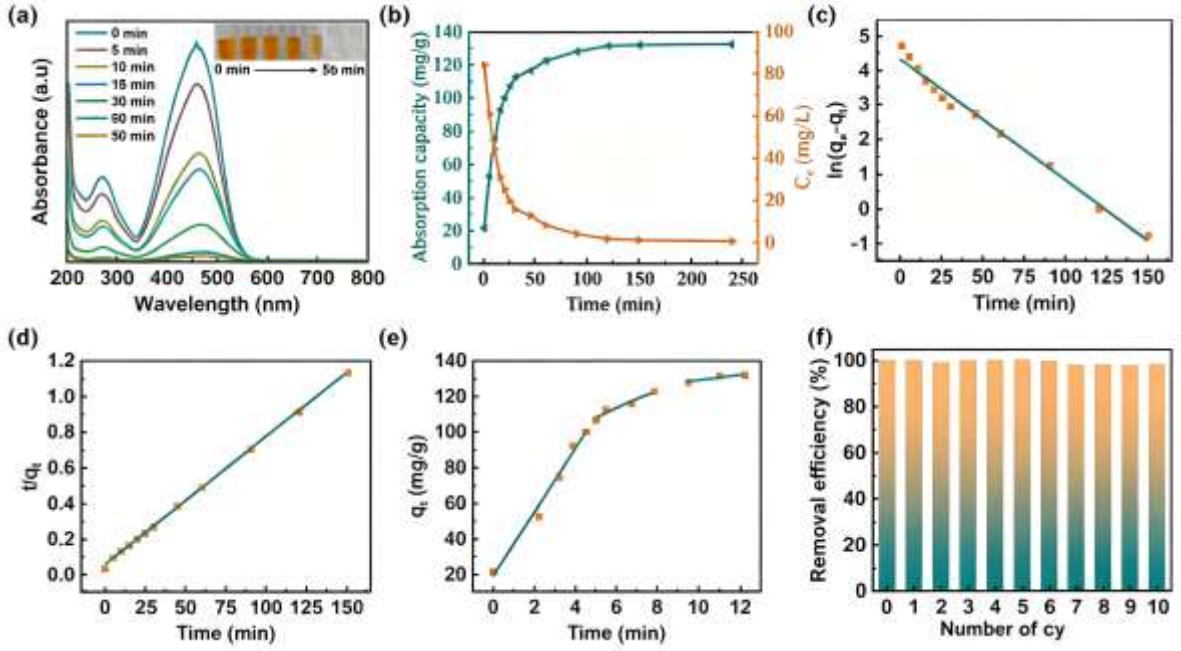

Figure 4 Dynamic adsorption characteristics of LSMs for methyl orange (a) UV-Vis spectra of the MO solution recorded at successive time intervals; (b) variation of adsorption capacity with contact time; (c) fit of the kinetic data to the pseudo-first-order model; (d) fit of the kinetic data to the pseudo-second-order model; (e) fitting curve based on the intra-particle diffusion model; (f) dye removal efficiency over repeated adsorption–desorption regeneration cycles

The intra-particle diffusion fit shown in Figure 4(e) resolves into three linear portions, which correspond to external surface diffusion, mesopore diffusion, and micropore diffusion, respectively. The diffusion rate constants follow the descending order ki1>ki2>ki3, which identifies surface diffusion as the fastest mass transfer event in the overall uptake sequence. Such a complex, stepwise adsorption pathway can be rationalized by the concurrent operation of several binding forces — electrostatic attraction, hydrogen bonding, π–π stacking, and van der Waals interactions — acting jointly between the LSMs and the MO molecules.

Table 1 Adsorption kinetic fitting parameters

Model Parameter	Pseudo-first-order	Pseudo-second-order
Experimental equilibrium capacity (qe) / (mg·g^{-1})	128.14	128.14
Fitted (qe) / (mg·g^{-1})	246.75	119.32
Rate constant k	-0.03497 min^{-1}	0.00721 g·mg^{-1}·min^{-1}
Correlation coefficient (R^2)	0.98398	0.99932

Table 2 Intra-particle diffusion model parameters

Stage	Parameter	Value
First stage	ki1	18.1562 mg·g^{-1}·min$^{-1/2}$
	Intercept ci1	18.1821
	R^2	0.98449
Second stage	ki2	5.1019 mg·g^{-1}·min$^{-1/2}$
	Intercept ci2	82.8582
	R^2	0.94933
Third stage	ki3	1.4541 mg·g^{-1}·min$^{-1/2}$
	Intercept ci3	114.7729
	R^2	0.86315

DOI:

3.4 Regenerative Cycling Performance

Recyclability is a critical index for evaluating the economic viability of adsorbents in industrial wastewater treatment. Dilute 0.1 mol·L^{-1} HCl ethanol solution was adopted as eluent to test the reusability of saturated LSM microspheres. After each adsorption run, MO-loaded LSMs were desorbed for 90 min in acidic ethanol, washed repeatedly with deionized water, dried and reused for the next cycle. As presented in Figure 4(f), after 10 successive cycles, the MO removal efficiency only drops from the initial level to 98.53%, with a total performance loss of merely 1.47%. The excellent cycling stability proves that the bio-based LSM microspheres possess great practical value for industrial dye wastewater disposal.

3.5 Adsorption Isotherms

To describe how MO molecules distribute themselves on the LSM surfaces once equilibrium is reached, the data were fitted with the Langmuir and Freundlich isotherm models, given in their nonlinear forms as Equation (6) and Equation (7):

$$q_e = \frac{q_{max} K_L C_e}{1 + K_L C_e} \quad (6)$$

$$q_e = K_F C_e^{\frac{1}{n}} \quad (7)$$

Where: qe: equilibrium adsorption capacity, mg·g^{-1}; qmax: theoretical monolayer saturation capacity, mg·g^{-1}; Ce: equilibrium residual MO concentration, mg·L^{-1}; KL: Langmuir adsorption constant, L·mg^{-1}; KF: Freundlich adsorption constant; n: heterogeneity factor representing adsorption favorability.

The equilibrium adsorption results in Figure 5(a) reveal that the adsorption capacity per unit mass rises steeply as the initial MO concentration increases, before leveling off once C0 exceeds 350mg/L. By fitting the equilibrium data in nonlinear form, the Langmuir and Freundlich plots presented in Figure 5(c) and (d) were obtained, and the parameters extracted from these fits are gathered in Table 3. The Langmuir description yields a markedly superior correlation coefficient R^2=0.99992, implying that MO is accommodated on the LSMs as a uniform monolayer. The monolayer saturation capacity deduced from this fit, 416.03 mg·g^{-1}, compares favorably with — and in most cases exceeds — the capacities reported for other methyl orange adsorbents in the literature (Table 4). Most comparative materials only function within narrow pH ranges, whereas LSMs maintain high uptake efficiency across pH 3–11 and 10–50 °C, demonstrating unique broad-spectrum advantages for practical wastewater treatment.

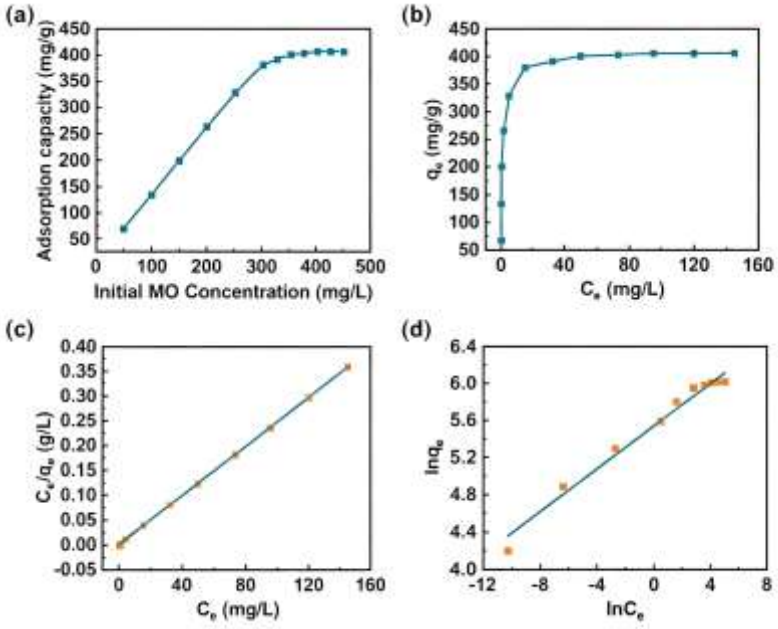

Figure 5 Adsorption isotherm characterization of LSMs for methyl orange (a) Adsorption capacity under different initial MO concentrations; (b) Equilibrium adsorption isotherm curve; (c) Langmuir model fitting; (d) Freundlich model fitting

Table 3 Adsorption isotherm fitting parameters

Langmuir Model	Value	Freundlich Model	Value
Q text max / ($mg \cdot g^{-1}$)	416.03	KF	1.12258
KL\/ ($L \cdot mg^{-1}$)	0.00245	1/n	0.66
Separation factor (RL	0.00103–0.00193	R2	0.97591
R2	0.99992	-	-

Table 4 Comparison of maximum MO adsorption capacity between LSMs and reported adsorbents

Adsorbent	Applicable pH	Temperature / °C	Q text max/ ($mg \cdot g^{-1}$)	Reference
Ni/NiO biochar	2	25	139.47	[29]
Palygorskite/UiO-66 composite	5	25	340.00	[30]
Magnetic Fe_3O_4@SiO_2 nanoparticles	2	45	182.53	[31]
Lignin-based Fe-MOF	3–11	25	195.31	[15]
Chitosan composite film	6–8	30	287.00	[11]
Waste cellulose-derived porous carbon	2.6	20	337.80	[12]
Lignin-zinc complex activated carbon	Not specified	50	263.60	[32]
Zinc ferrite loaded hydroxyethyl cellulose/chitosan film	6–8	Not specified	288.00	[33]
This work (LSM microspheres)	3–11	10–50	416.03	Present study

3.6 Adsorption Mechanism Analysis

FTIR and XPS characterizations of LSMs before and after MO saturation were conducted to clarify the intrinsic adsorption interactions. As illustrated in Figure 6(a), the C–N stretching band at 1460 cm^{-1} remains observable on both pristine and loaded LSMs, which originates from electrostatic attraction between protonated amine groups on LSMs and anionic MO molecules. The aromatic C=C peak shifts from 1660 cm^{-1} to 1605 cm^{-1}, and the broad O–H vibration band at 3386 cm^{-1} migrates to 3304 cm^{-1} after dye loading, which provides direct evidence of π-π stacking and intermolecular hydrogen bonding between LSM and MO aromatic frameworks.

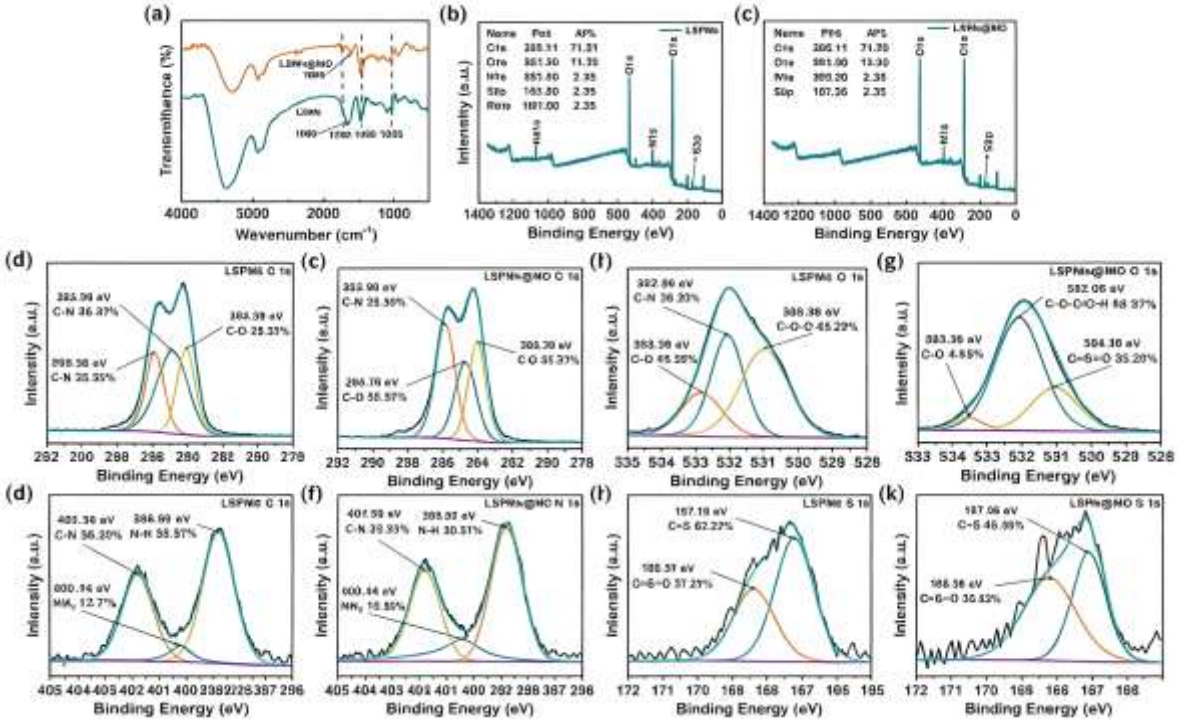

Figure 6 Comparative XPS and FTIR analyses of the LSMs prior to and following MO uptake (a) FTIR spectra of pristine and MO-loaded LSMs; (b) Full XPS spectrum of raw LSMs; (c) Full XPS spectrum of MO@LSM; (d,e) C 1s high-resolution spectra; (f,g) O 1s high-resolution spectra; (h,i) N 1s high-resolution spectra; (j,k) S 2p high-resolution spectra

Full XPS spectra (Figure 6(b), (c)) reveal elevated atomic percentages of oxygen (17.18% → 18.61%) and sulfur (2.38% → 2.76%) on MO-saturated LSMs, confirming successful immobilization of MO molecules on microsphere surfaces. High-resolution C 1s spectra (Figure 6(d), (e)) show slight binding energy shifts of C–C, C–N and C–O components after adsorption, which is attributed to π-π electronic coupling between the aromatic rings of LSM and MO.

In the O 1s region (Figure 6(f), (g)), the pristine LSMs display two resolvable signals — one at 530.96 eV attributed to C–O–C and another at 532.04 eV arising from hydroxyl O–H — whereas after MO capture these collapse into one broad feature at 532.05 eV; concurrently, the C–O signal undergoes a red shift, moving from 532.98 eV to 533.54 eV. A new signal at 531.04 eV assigned to the sulfonate O=S=O groups of MO emerges on loaded samples, further verifying MO attachment. The N 1s peaks (Figure 6(h), (i)) of amine functional groups shift toward higher binding energies after dye adsorption, demonstrating electron cloud rearrangement induced by electrostatic attraction and hydrogen bonding interactions. In S 2p spectra (Figure 6(j), (k)), the C=S peak shifts from 167.19 eV to 167.06 eV and the O=S=O band moves from 168.37 eV to 168.18 eV, which originates from hydrogen bonds formed between MO sulfonate groups and LSM amine sites.

Collectively, FTIR and XPS results corroborate that the adsorption of MO onto PEI-grafted lignin microspheres is a synergistic process governed by four intermolecular forces: electrostatic attraction, hydrogen bonding, π-π stacking and van der Waals interactions. A schematic diagram illustrating the comprehensive adsorption mechanism is presented in Figure 7. Protonated amine groups on LSM surfaces carry positive charges, while MO dissociates into negatively charged sulfonate anions over pH 3–11, generating strong electrostatic driving force for fast dye capture. Meanwhile, the aromatic skeletons, amine and sulfonate groups of the two substances form hydrogen bonds and π-π stacking interactions, jointly enhancing the overall adsorption capacity of the bio-based microspheres within the broad pH window.

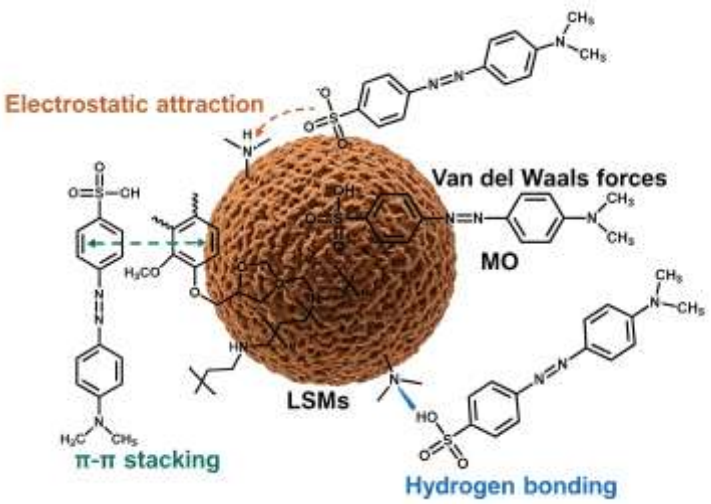

Figure 7 Schematic illustration of the adsorption mechanism between LSM microspheres and methyl orange

In this study, bio-based polyethyleneimine-grafted sodium lignosulfonate microspheres (LSMs) were synthesized via inverse suspension polymerization to address key drawbacks of conventional adsorbents, including narrow pH adaptability, poor reusability and limited adsorption capacity for anionic methyl-orange (MO) dye. The prominent adsorption performance of LSMs originates from combined structural modification, abundant surface functional groups and multiple synergistic intermolecular interactions.

Raw sodium lignosulfonate suffers from severe particle aggregation caused by intra- and intermolecular hydrogen bonds, which yields low specific surface area and insufficient accessible active sites, restricting its dye-removal capability. Through inverse suspension copolymerization with polyethyleneimine (PEI) using epichlorohydrin as cross-linker, the prepared LSM microspheres achieve uniform particle size and well-dispersed spherical morphology without obvious stacking. Such textured surface topography greatly enlarges the contact area between adsorbent and dye molecules and facilitates mass transfer and molecular diffusion. Spectroscopic characterizations confirm successful grafting of PEI chains onto lignosulfonate backbones: new C-N stretching signals in FTIR spectra and the appearance of nitrogen element in XPS full-scan spectra verify the introduction of massive amine functional groups from PEI. Thermogravimetric tests further demonstrate that PEI accounts for approximately 51.85 % of the composite mass, supplying high-density amine sites on microsphere surfaces.

The introduced amine groups are primarily responsible for the broad-pH adsorption advantage. Zeta-potential measurements show the isoelectric point of LSMs reaches 10.6. Within pH 3-11, the surface amines become protonated and carry positive charges, whereas methyl orange exists as negatively-charged anionic species. Strong electrostatic attraction thus drives fast capture of MO molecules across this wide pH window, overcoming the narrow working-pH limitation of many reported lignin-derived adsorbents. Even under fluctuating temperature conditions from 10 °C to 50 °C, LSMs maintain stable removal efficiency because thermal motion accelerates molecular collision without destroying the surface functional structure.

Kinetic fitting reveals that the pseudo-second-order model best describes the adsorption process, indicating chemical-interaction-dominated rate-limiting behaviour. Intra-particle-diffusion modelling demonstrates a multi-stage mass-transfer process: rapid external-surface adsorption occupies most dye uptake within the initial 45 min, followed by gradual mesopore and micropore diffusion. Beyond electrostatic attraction, FTIR and high-resolution XPS spectra prove that hydrogen bonding, π-π stacking and van der Waals forces jointly contribute to MO sequestration. Aromatic skeletons from both LSMs and MO generate π-π electronic coupling, while hydroxyl, sulfonate and protonated amine sites form plentiful intermolecular hydrogen bonds. These non-covalent forces cooperate rather than acting independently, substantially raising the monolayer saturated adsorption capacity up to 416.03 $mg \cdot g^{-1}$ according to Langmuir isotherm fitting.

Moreover, the cross-linked three-dimensional network structure endows LSMs with outstanding regenerability. After ten consecutive adsorption-desorption cycles using acidic ethanol eluent, the MO removal efficiency only decreases by 1.47 %. This stable cycling performance is attributed to reversible non-covalent binding between LSM active sites and MO anions; dye molecules can be readily stripped without irreversible damage to grafted-PEI functional sites or microsphere architecture. In summary, inverse-suspension grafting modification optimizes particle dispersion and introduces high-density amine sites. The synergism of electrostatic attraction, hydrogen bonding, π-π stacking and van der Waals interactions realizes high-capacity, wide-pH and recyclable dye removal, making LSMs promising sustainable adsorbents for practical textile-industry wastewater remediation.

4 Conclusions

Amine-functionalized sodium lignosulfonate microspheres (LSMs) were successfully fabricated via inverse suspension polymerization using sodium lignosulfonate as the main matrix and polyethyleneimine as the functional grafting monomer. This work expands the high-value utilization pathway of lignin for organic dye wastewater remediation.

Owing to their rugged surface topography and an abundance of protonated amine functionalities, the as-obtained LSM microspheres are capable of sequestering methyl orange with high efficiency over an extended pH interval of 3–11, delivering a monolayer saturation capacity as high as 416.03 $mg \cdot g^{-1}$.

Close agreement with both the Langmuir monolayer isotherm and the pseudo-second-order kinetic model reveals that chemisorption constitutes the principal pathway through which MO is bound to the LSMs. Even upon completion of ten adsorption–desorption rounds, the dye removal efficiency drops by only 1.47%, underscoring the adsorbent's remarkable regeneration capability.

The bio-based LSM microspheres synthesized in this study are simple to prepare, highly efficient and pH-tolerant adsorbents with promising industrial application potential for organic dye wastewater treatment and environmental protection.

References

[1] Liu W, Dai C, He L H, et al. Biomass aerogel: An emerging eco-friendly material for adsorbing pollutants in water[J]. Chemical Engineering Journal, 2024, 513: 162977.

[2] Ojike C A, Hagen V, Beszteri B, et al. Surface-functionalized diatoms as green nano-adsorbents for the removal of methylene blue and methyl orange as model dyes[J]. Advanced Sustainable Systems, 2024, 9(3): 2400776.

[3] Hussain M H A, Soylu G S P. Metal oxide nanoparticles synthesized in ionic liquids: Characterization and photodegradation of methyl orange[J]. ACS Omega, 2024, 10(10): 9962-9975.

[4] Pandit S, Yadav N, Sharma P, et al. Life cycle assessment and techno-economic analysis of nanotechnology-based wastewater treatment: Status, challenges and future prospectives[J]. Journal of the Taiwan Institute of Chemical Engineers, 2024, 166: 105567.

[5] Wu H Y, Gong L, Zhang X, et al. Bifunctional porous polyethyleneimine-grafted lignin microspheres for efficient adsorption of 2,4-dichlorophenoxyacetic acid over a wide pH range and controlled release[J]. Chemical Engineering Journal, 2021, 411: 128539.

[6] Marey A, Gado W S, Soliman A G, et al. Efficient removal of methylene blue dye from wastewater specimen using polystyrene coated nanoparticles of silica[J]. Inorganic Chemistry Communications, 2024, 160: 112018.

[7] Castaldo R, Avolio R, Cocca M, et al. Amino-functionalized hyper-crosslinked poly(vinylbenzyl chloride-divinylbenzene) resins for enhanced adsorption of polar dyes and CO_2[J]. Chemical Engineering Journal, 2021, 418: 129463.

[8] Lin W J, Wu S, Han S B, et al. Preparation and characterization of highly conductive lignin aerogel based on

tunicate nanocellulose framework[J]. International Journal of Biological Macromolecules, 2023, 242: 125010.

[9] Lu W J, Zhang C H, Li Y X, et al. Double cross-linked chitosan sponge embedded ZrO-soy protein amyloid nanoparticles for fluoride removal[J]. International Journal of Biological Macromolecules, 2024, 279: 135520.

[10] Lin W J, Ning D W, Zou Q X, et al. Preparation and properties of flame-retardant thermal insulation tunicate cellulose aerogel[J]. China Pulp & Paper, 2023, 42: 20-30.

[11] Hussain S, Kamran M, Khan S A, et al. Adsorption, kinetics and thermodynamics of methyl orange on chitosan composite films[J]. International Journal of Biological Macromolecules, 2021, 168: 383-394.

[12] Sun B F, Yuan Y N, Li H L. Waste cellulose derived porous carbon for methyl orange removal[J]. Chemical Engineering Journal, 2019, 371: 55-63.

[13] Wang C, Feng X Z, Zhang H B. Progress on preparation and application of lignin-based adsorbents[J]. Chemical Reagents, 2023, 45(04): 120-127.

[14] Lin W J, Ning D W, Xu D Z. Effects of free and bound lignin on cellulose enzymatic hydrolysis[J]. Industrial Crops and Products, 2024, 222: 119516.

[15] Wang C, Feng X Z, Tian Y B. Facile synthesis of lignin Fe-MOF for rapid methyl orange adsorption[J]. Environmental Research, 2024, 251: 118651.

[16] Wan Y L, Hu Y L, Xu D X. Fabrication and UV-shielding performance of cellulose/lignin microsphere composite films[J]. Journal of Materials Engineering, 2021, 49: 56-63.

[17] Popović A L, Rusmirović J D, Veličković Z, et al. Novel amino-modified lignin microspheres as high-capacity biosorbents for heavy metal sequestration[J]. International Journal of Biological Macromolecules, 2020, 156: 1160-1173.

[18] Gao X P, Li M. Comment on green porous lignin spheres for lead ion removal[J]. Journal of Hazardous Materials, 2019, 364: 537-538.

[19] Ge Y Y, Cui X M, Liao C L. Green geopolymer-alginate hybrid spheres for Cu(II) removal: Batch and column tests[J]. Chemical Engineering Journal, 2017, 311: 126-134.

[20] Kong Y, Wang L, Ge Y Y. Lignin xanthate-bentonite composite adsorbent for doxycycline and mercury ion elimination[J]. Journal of Hazardous Materials, 2019, 368: 33-41.

[21] Gao J, Wang Z Q, Li B. Hydrothermal pH effect on lignin porous carbon microspheres and CO_2 adsorption mechanism[J]. Bioresource Technology, 2024, 393: 130171.

[22] Annadurai G, Juang R S, Lee D J. Dye adsorption using cellulose waste materials[J]. Journal of Hazardous Materials, 2002, 92(3): 263-274.

[23] Zhang S Y, Dai F N, Wang Q. PEG-templated porous hollow polysulfone microspheres for methylene blue adsorption[J]. Colloids and Surfaces A, 2022, 634: 127949.

[24] Zhang L H, Gao M, Guo S. Carboxyl-functional PMMA microspheres for methylene blue adsorption[J]. Journal of Materials Engineering, 2024, 53(02): 219-226.

[25] Pimentel C H, Freire M S, Gómez-Díaz D. Dye removal by raw pine sawdust[J]. Cellulose, 2023, 30(7): 4587-4608.

[26] Gök Ö, Özcan A, Erdem B. Adsorption parameter prediction for 8-hydroxyquinoline immobilized bentonite[J]. Colloids and Surfaces A, 2008, 317: 174-185.

[27] Langmuir I. Adsorption of gases on glass, mica and platinum surfaces[J]. Journal of the American Chemical Society, 1918, 40: 1361-1403.

[28] Pang Y X, Lin P Y, Chen Z S. Porous polyamine lignin microspheres: Preparation and adsorption performance[J]. International Journal of Biological Macromolecules, 2023, 253: 127026.

[29] Mon P P, Cho P P, Chandana L. Ni/NiO modified biowaste biochar for methyl orange adsorption[J]. Journal of Environmental Management, 2023, 344: 118418.

[30] Vasiliadou I A, Ioannidou T, Anagnostopoulou M. Palygorskite/UiO-66 composite for methyl orange removal[J]. Applied Sciences, 2022, 12(15): 7468.

[31] Li H, Jin H H, Li R R. Adsorption behavior of magnetic Fe_3O_4@SiO_2 nanoparticles toward methyl orange[J]. Scientific Reports, 2024, 14(1): 1217.

[32] Wang L L, Wang G H, Sui W J. High-capacity activated carbon prepared via lignin-zinc complex from black liquor[J]. Transactions of China Pulp and Paper, 2023, 38(02): 1-11.

[33] Abdelaziz M M, Abdelaziz M A, Omer N. Zinc ferrite functionalized hydroxyethyl cellulose/chitosan film for methyl orange removal[J]. International Journal of Biological Macromolecules, 2024, 307: 142232.

[34] Lin W J, Han H, Yan X L. Lignin-reinforced polypyrrole hydrogel for supercapacitor and sensing electrodes[J].

International Journal of Biological Macromolecules, 2024, 273: 132962.

[35] Qu W, He D L, Huang H H. Amino-crosslinked hypromellose for methyl orange adsorption[J]. Journal of Materials Science, 2020, 55(17): 7268-7282.

[36] Kert M, Skoko J. pH-responsive cotton fiber modified by methyl orange adsorption[J]. Polymers, 2023, 15(7): 1783.